Elliptic and Triangular Flow of Identified Particles from the AMPT Model at RHIC Energies

Xu Sun,[1] Jianli Liu,[1] Alexander Schmah,[2] Shusu Shi,[3] Jingbo Zhang,[1] Hanzhi Jiang,[4] and Lei Huo[1, *]

[1]*Department of Physics, Harbin Institute of Technology, Harbin 150001, China*
[2]*Nuclear Science Division, Lawrence Berkeley National Laboratory, Berkeley, California 94720, USA*
[3]*Key Laboratory of Quarks and Lepton Physics (MOE) and Institute of Particle Physics,*
Central China Normal University, Wuhan, 430079, China
[4]*School of Astronautics, Harbin Institute of Technology, Harbin 150001, China*
(Dated: September 28, 2015)

The elliptic flow (v_2) at $\sqrt{s_{NN}} = 11.5$, 39, and 200 GeV and triangular flow (v_3) at $\sqrt{s_{NN}} = 200$ GeV of identified particles ($\pi^\pm, K^\pm, K_S^0, p, \bar{p}, \phi, \Lambda$ and $\bar{\Lambda}$) from 0%–80% central Au+Au collisions are analyzed using a multiphase transport (AMPT) model. It is shown that the experimental results from the η-sub event plane method can be reproduced with a parton scattering cross section between 1.5 and 3 mb. We also studied the differential and integrated v_2/v_3 ratios and conclude that they are anti-correlated with the parton scattering cross section.

PACS numbers: 25.75.-q, 25.75.Ld

I. INTRODUCTION

One of the main goals of heavy-ion collision experiments at the Relativistic Heavy Ion Collider (RHIC) is to study the properties and formation of the Quark Gluon Plasma (QGP). The study of the azimuthal anisotropy of emitted particles, based on Fourier decomposition, is considered to be one of the most important tools to investigate the hot and dense matter created in heavy-ion collisions [1]. Several interesting observations of the second harmonic Fourier coefficient v_2, also called elliptic flow, have been reported during the past decade by using the data from the top RHIC heavy-ion energy of $\sqrt{s_{NN}} = 200$ GeV [2–4]. At low transverse momenta ($p_T < 2.0$ GeV/c), a mass ordering of $v_2(p_T)$ was observed [5, 6], which can be understood within a hydrodynamic framework [7]. At intermediate transverse momenta ($2.0 < p_T < 6.0$ GeV/c), a Number-of-Constituent Quark (NCQ) scaling [8] was observed [9–12]. The NCQ scaling was used to conclude that the relevant degrees of freedom in the created matter are quarks and gluons. In addition to measurements at top RHIC energies, a Beam Energy Scan (BES) program has been carried out in the years 2010, 2011 and 2014 at to study the structure of the QCD phase diagram. Au+Au collisions were recorded at $\sqrt{s_{NN}} = 7.7$, 11.5, 14.5, 19.6, 27, 39, and 62.4 GeV. The mass ordering in the low p_T region and NCQ scaling at intermediate transverse momenta were also observed BES energies [13, 14].

In the recent years, the third harmonic Fourier coefficient v_3, called triangular flow, has attracted more attention and was studied intensively [15, 16]. It is thought to be related to the near-side ridge structure observed in two particle correlation measurements [15]. The triangular flow seems to be more sensitive to the viscous effects than v_2 [17], but less sensitive to the collision centrality [18]. Thus, v_3 is a natural choice to study initial fluctuations and viscosity effects. Similar flow patterns as for v_2 were recently observed in v_3 measurements [19, 20].

Viscous relativistic hydrodynamic calculations [21, 22] suggest a combined analysis of elliptic and triangular flow data to put tight constraints on the initial states of nucleus-nucleus collisions. Other hydrodynamic model calculations [23] predict a stronger damping of the higher harmonic flow coefficients (n > 2) relative to v_2 at high transverse momenta. A constant ratio of $v_2(p_T)/v_3(p_T)$ at high p_T is predicted, where high means $p_T/m_T > \bar{v}_{max}$ and $\bar{v}_{max}$ is the highest flow velocity. Thus, by combining elliptic and triangular flow, more information about the initial state and the influence of the viscous effect can be collected.

In this paper, the differential and integrated ratio of v_2/v_3 of identified particles ($\pi^\pm, K^\pm, K_S^0, p, \bar{p}, \phi, \Lambda$ and $\bar{\Lambda}$) are studied with the AMPT model. This paper is organized as follows. Section II gives a brief introduction to the η-sub event plane method and the AMPT model. In section III A, the collective flow calculations (v_2 and v_3) from the AMPT model are presented. The differential and integrated v_2/v_3 ratios are discussed in Sec. III B and Sec. III C. A summary is given in Sec. IV.

II. η-SUB EVENT PLANE METHOD AND THE AMPT MODEL

A. η-sub Event Method

The event plane method is one of the most widely used methods to analyze anisotropic flow in heavy-ion collisions [24]. In non-central Au+Au collision, the overlap region has an almond shape in the coordinate space. As the system evolves, the pressure gradient pushes the anisotropy from coordinate space to momentum space,

therefore the produced particles have an anisotropic distribution in momentum space. The azimuthal distribution of the produced particles can be written as [25]:

$$E\frac{d^3N}{dp^3} = \frac{1}{2\pi}\frac{d^2N}{p_{\mathrm{T}}dp_{\mathrm{T}}dy}(1+\sum_{n=1}^{\infty}2v_n^{\mathrm{obs}}\cos[n(\phi-\Psi_n)]), \quad (1)$$

where ϕ is the azimuthal angle of a particle, v_n^{obs} is the observed n-th harmonic flow., and Ψ_n is the n-th harmonic event plane angle reconstructed by the produced particles, defined as:

$$\Psi_n = \frac{1}{n}[\tan^{-1}\frac{\sum_i w_i \sin(n\phi_i)}{\sum_i w_i \cos(n\phi_i)}]. \quad (2)$$

The sum goes over all charged particles in the event, w_i is a weight applied to optimize the event plane resolution, see [24] for details. It is worth to note that the range of n-th harmonic event plane angle is $0 \leqslant \Psi_n < 2\pi/\mathrm{n}$.

In this method the n-th observed harmonic flow can be corrected for statistical effects by the n-th harmonic event plane resolution:

$$v_n = v_n^{obs}/R_n, \quad (3)$$

with

$$R_n = \langle \cos[n(\Psi_n - \Psi_{nR})]\rangle. \quad (4)$$

Here $\langle\ldots\rangle$ denotes the average over all particles in all events and Ψ_{nR} is the n-th real event plane angle [26]. The real event plane means the participant plane [27], which can not be achieved due to finite multiplicity of an event.

To reduce the short range "non-flow" effects such as HBT correlations, a η-sub event plane method was introduced [14]. The η-sub event plane method divides the event into two independent sub-events with different pseudo rapidity (η) ranges. An additional gap of 0.1 in pseudo rapidity is added to further avoid short range correlations. The procedure results in a positive and negative η-sub event plane. The n-th observed harmonic flow can now be calculated in respect to the η-sub event planes. As a consequence, the η-sub event plane resolution [24] is used instead of full event plane resolution:

$$R_n^{sub} = \sqrt{\langle\cos[n(\Psi_n^a - \Psi_n^b)]\rangle}, \quad (5)$$

where the Ψ_n^a and the Ψ_n^b are the n-th harmonic event plane angles for the positive and negative η-sub ranges.

B. AMPT Model

AMPT is a transport model which consists of four main components: the initial conditions, partonic interactions, conversion from partonic to hadronic matter, and hadronic interactions [28]. It has two versions to deal with different scenarios which are default

AMPT (AMPT Def in following figures) and string melting AMPT (AMPT Str in following figures). The initial conditions are generated by the HIJING (Heavy Ion Jet Interaction Generator) model [29–31]. HIJING includes only two body nucleon-nucleon interactions and generates mini jets and excited strings through hard processes and soft processes separately.

Excited strings are treated differently in the two AMPT versions. In default AMPT, excited strings are combined to hadrons according to the Lund string fragmentation model they further go through a hadronic interaction stage [28]. In string melting AMPT, excited strings first convert to partons, i.e. melting, and then go through a partonic interaction stage with original soft partons. The partonic interactions for both default AMPT and string melting AMPT are described by ZPC (Zhang's Parton Cascade) model [32]. In the final stage of the ZPC model, partons in default AMPT are recombined with parent strings and hadronize via the Lund string fragmentation model. However, in string melting AMPT, the hadronization of partons is described by a coalescence model. After hadronization, the hadronic interactions are modelled by ART (A Relativistic Transport) model [33, 34].

In previous studies it was found that a large parton scattering cross section (approximately 6 mb or 10 mb) is needed to reproduce the observed elliptic flow of charged hadrons [35, 36]. In these studies, the elliptic flow was calculated with respect to the reaction plane (determined by the beam axis and impact parameter direction), which is 0 in the AMPT model, and this might underestimate the elliptic flow observed in the experiment data, which measured relative to the event plane but not the reaction plane [24]. As shown in Ref. [37], both the charged particle multiplicity and elliptic flow can be reproduced with a smaller parton scattering cross section (1.5 mb) by using the default values for the parameters in the Lund string fragmentation function.

In this paper, approximately 20 million events for 0%–80% central Au+Au collisions at $\sqrt{s_{\mathrm{NN}}} = 11.5$, 39, and 200 GeV with default AMPT (v1.25) and string melting AMPT (v2.25) were generated. Three different parton scattering cross sections (1.5 mb, 3 mb, and 6 mb) are used in the string melting version of AMPT. The parameters in the Lund string fragmentation function are set to the default values for AMPT with 1.5 mb parton scattering cross section (the values can be found at Table I in Ref. [37]). Furthermore the η-sub event plane method is used to calculate elliptic and triangular flow.

III.   RESULTS

Identical analysis steps are used for simulation and data collected from the experiments [14, 20]. Finial state charged particles with $0.2 < p_{\mathrm{T}} < 2.0$ GeV/c and $|\eta| < 1.0$, are used to reconstruct the event plane. The η range of the two $\eta-$sub events are $-1.0 < \eta < -0.05$ and 0.05
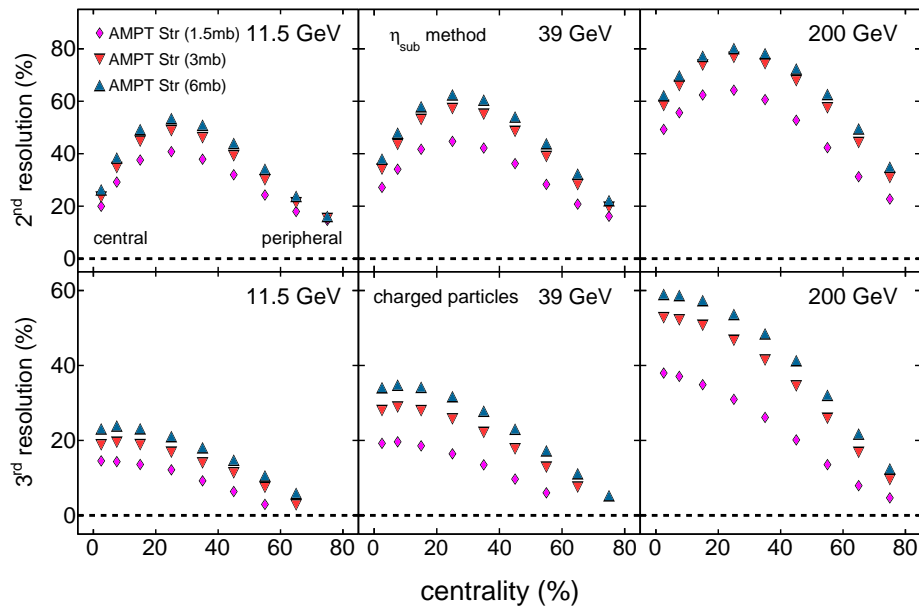
FIG. 1. (Color online) Second harmonic (top panel) and third harmonic (bottom panel) event plane resolution from the AMPT string melting model with 1.5 mb (AMPT Str (1.5 mb)), 3 mb (AMPT Str (3 mb)) and with 6 mb (AMPT Str (6 mb)) parton scattering cross section from 0%-80% central Au+Au collisions at $\sqrt{s_{NN}} = 11.5$, 39 and 200 GeV. The analysis method is η-sub event plane method, and the event plane is reconstructed by charged particles, see text for details.

$< \eta < 1.0$, respectively. The elliptic and triangular flow are calculated within -1.0 $< \eta <$ 1.0, and the auto-correlation is naturally avoided by the η-sub event plane method. For all the plots in this section, only statistical errors are shown.

A. Elliptic Flow and Triangular Flow at RHIC

Figure 1 presents the second and third harmonic event plane resolutions from the AMPT string melting model for parton scattering cross sections of 1.5 mb, 3 mb and 6 mb from 0%-80% central Au+Au collisions at $\sqrt{s_{NN}} =$ 11.5, 39 and 200 GeV by using the η-sub event plane method. The event plane resolution shows a clear parton scattering cross section and energy dependence: both second and third harmonic event plane resolution increases with increasing parton scattering cross section and energy.

The third harmonic event plane resolution is about two times smaller and peaks more central than the second harmonic event plane resolution, which is comparable to the one from experiment. For $\sqrt{s_{NN}} =$ 11.5 and 39 GeV, v_3 can only be calculated up to 0%–60% (0%–70%) for some of the parton scattering cross sections, since we only have event plane resolution up to these centrality.

Figure 2, Fig. 3 and Fig. 4 show the comparison between data from experiment and from the AMPT model for $v_2(p_T)$ of identified particles ($\pi^\pm, K^\pm, p, \bar{p}$ and ϕ)

at $\sqrt{s_{NN}} =$ 11.5, 39 and 200 GeV from 0%–80% central Au+Au collisions. The data from experiment are taken from Ref. [14, 38]. For all three energies it is observed that the elliptic flow increases with increasing parton scattering cross section. The elliptic flow from default AMPT is lower than the corresponding results from experiment, which indicates that the parton scattering process is important to produce a large elliptic flow as observed in experiment data. Previous studies show that a 6-10 mb parton scattering cross section is needed to reproduce the elliptic flow observed in experiment data [35, 36]. In those studies the elliptic flow was calculated relative to the reaction plane.

By using the η-sub event plane method most of the experiment data points at low transverse momenta are between AMPT default and AMPT string melting with a 3 mb parton scattering cross section. At intermediate p_T some particle species, e.g. $\pi^\pm$, are systematically above AMPT string melting with a 3 mb parton scattering cross section. That means previous studies have underestimated the elliptic flow by using the reaction plane instead of the event plane. Latter one fluctuates event-by-event around the reaction plane. The collective flow measured in experiment are not mean values, but closer to a root-mean-sqaure [39], therefore, the event-by-event fluctuations did not cancel each other but give a positive contribution to the measured collective flow, which makes the collective flow relative to the event plane is always larger compare to the collective flow relative to
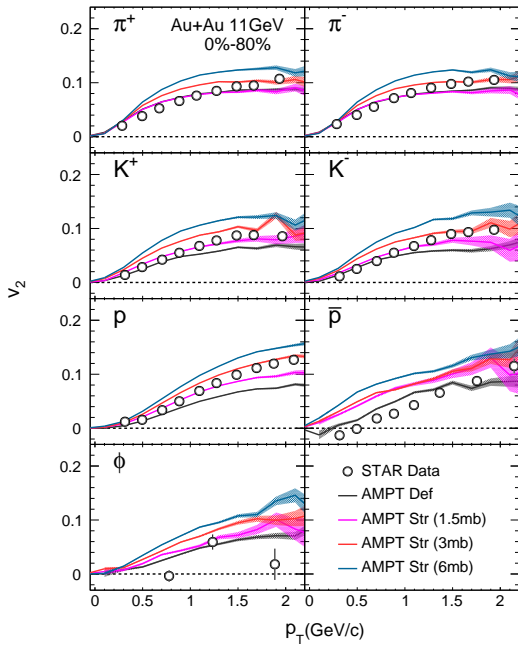
FIG. 2. (Color online) $v_2(p_T)$ results at $\sqrt{s_{NN}} = 11.5$ GeV from 0%–80% central Au+Au collisions for identified particles ($\pi^{\pm}, K^{\pm}, p, \bar{p}$ and ϕ) in comparison to STAR data.
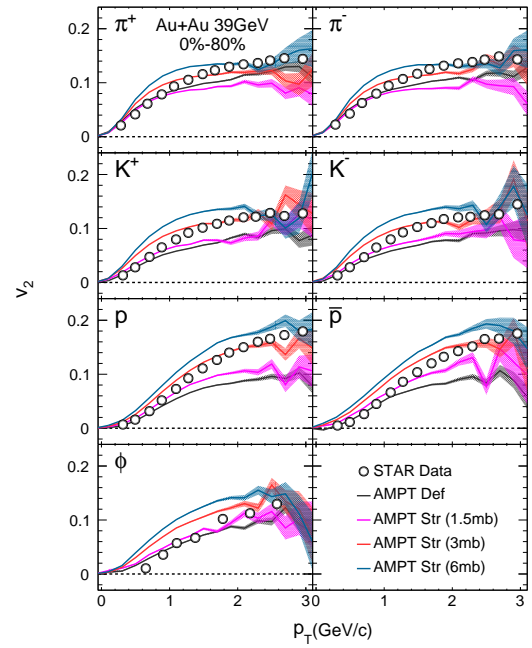

FIG. 3. (Color online) $v_2(p_T)$ results at $\sqrt{s_{NN}} = 39$ GeV from 0%–80% central Au+Au collisions for identified particles ($\pi^{\pm}, K^{\pm}, p, \bar{p}$ and ϕ) in comparison to STAR data.
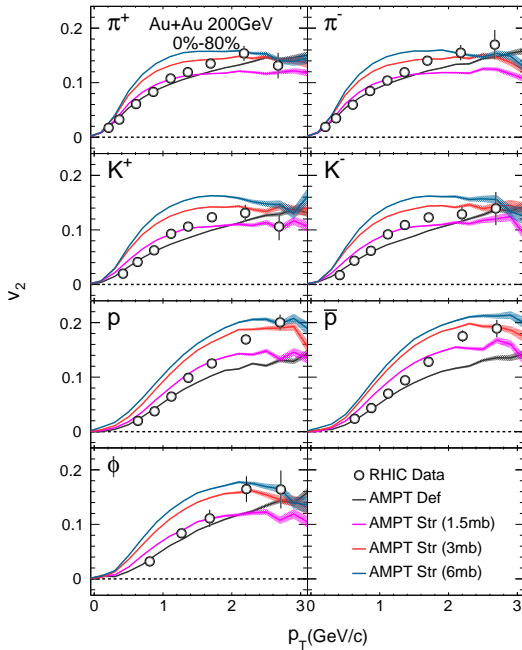

FIG. 4. (Color online) $v_2(p_T)$ results at $\sqrt{s_{NN}} = 200$ GeV from 0%–80% central Au+Au collisions for identified particles ($\pi^{\pm}, K^{\pm}, p, \bar{p}$ and ϕ) in comparison to RHIC data. The open symbols in the panels of $\pi^{\pm}, K^{\pm}, p$ and $\bar{p}$ are from PHENIX [38] and the panel of ϕ are from STAR [10] and the lines are from AMPT calculation.
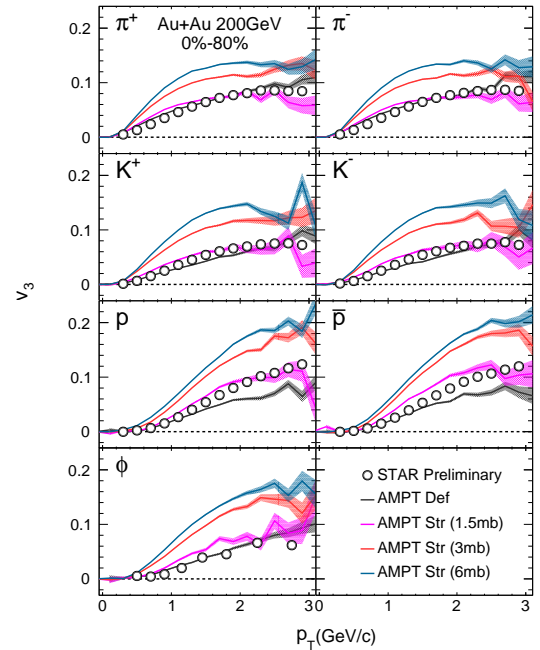

FIG. 5. (Color online) $v_3(p_T)$ results at $\sqrt{s_{NN}} = 200$ GeV from 0%–80% central Au+Au collisions for identified particles ($\pi^{\pm}, K^{\pm}, p, \bar{p}$ and ϕ) in comparison to STAR data.

the reaction plane.

Figure 5 shows the comparison between experiment data [20] and AMPT model calculations for $v_3(p_T)$ at

$\sqrt{s_{\mathrm{NN}}} = 200$ GeV from 0%–80% central Au+Au collisions of identified particles ($\pi^{\pm}, K^{\pm}, p, \bar{p}$ and ϕ). A similar parton scattering cross section dependence is observed as for the elliptic flow, but here the dependence is stronger: v_3 is about 40% lower than v_2 with 1.5 mb parton scattering cross section but comparable with v_2 with a 6 mb parton scattering cross section. The driving force behind v_2 is the almond shape of initial nuclei overlap region, therefore, v_2 has a relative large value compare to v_3 which is mainly generated by initial state fluctuations [15]. This effect can be observed by comparing the v_2 and v_3 values from AMPT default model calculations in Fig. 4 and Fig. 5. The higher parton scattering cross section makes the transportation from the initial coordinate space to the final momentum space more efficient, which increases the values for both v_2 and v_3. The relative increase of v_3 is larger than for v_2, since the effects of the parton scattering is more important for v_3. The triangular and elliptic flow from experiment can be well reproduced by AMPT default and AMPT string melting with a 1.5 mb parton scattering cross section, see Fig. 4 and Fig. 5. It is worth to be noticed here that we did not find out a single parton scattering cross section to describe all particle species. This is because the collective flow results from AMPT model depend on both the magnitude and the distribution of parton scattering cross section. Recent analysis [37] showed that the experiment elliptic flow results can be described by the string melting AMPT model with a smaller but more isotropic parton scattering cross section. Thus, by carefully tuning the parton scattering cross section and its distribution, we might achieve a roughly description of all parton species, but this is beyond the goal of this paper.

B. Differential $v_2(p_{\mathrm{T}})/v_3(p_{\mathrm{T}})$ Ratio from AMPT Model

Figure 6 depicts AMPT model calculations for the transverse momentum dependent differential ratio $v_2(p_{\mathrm{T}})/v_3(p_{\mathrm{T}})$ for identified particles ($\pi^{\pm}, K^{\pm}, K_s^0, \phi, p, \bar{p}, \Lambda$ and $\bar{\Lambda}$) from 0%–80% central Au+Au collisions at $\sqrt{s_{\mathrm{NN}}} = 200$ GeV. The differential ratio decreases significantly at low transverse momenta ($p_{\mathrm{T}} < 1.5$ GeV/c) and becomes flat at intermediate transverse momenta ($1.5 < p_{\mathrm{T}} < 3.0$ GeV/c). The p_{T} dependent differential ratio shows an anti-correlation with parton scattering cross section for all particle species: the higher the parton scattering cross section, the lower the $v_2(p_{\mathrm{T}})/v_3(p_{\mathrm{T}})$ ratio. This is in agreement with a larger increase of v_3 with increasing parton scattering cross section compare to v_2 discussed in Fig. 4 and Fig. 5. This effect can also be understood in a hydrodynamic frame work. The higher parton scattering cross section in the AMPT string melting model is equivalent to a lower viscosity in viscous hydrodynamics [40, 41]. From this study it is known that v_3 is more sensitive to viscosity than v_2 [17], therefore a lower

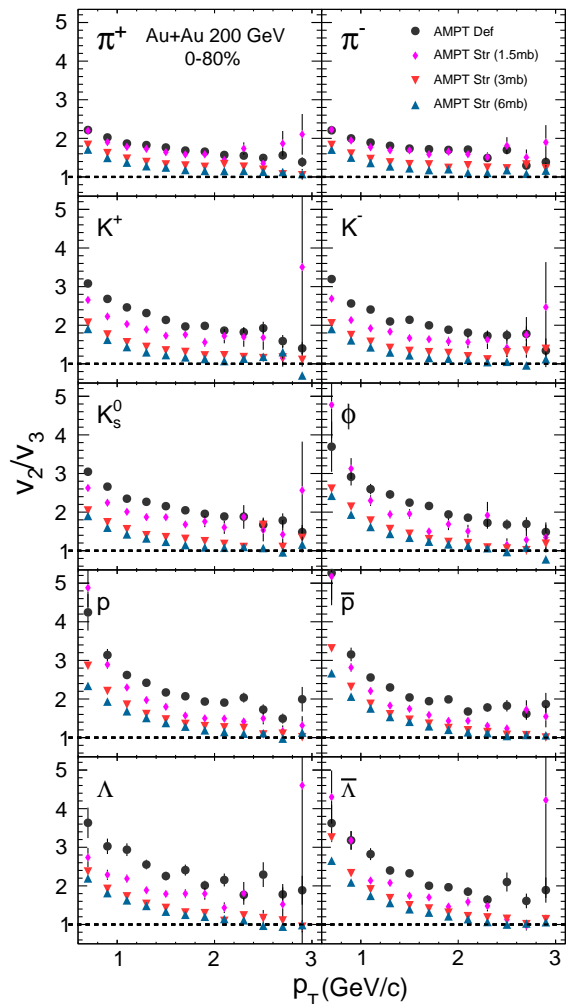viscosity (higher parton scattering cross section) leads to a lower $v_2(p_{\mathrm{T}})/v_3(p_{\mathrm{T}})$ ratio.

FIG. 6. (Color online) AMPT calculation of differential $v_2(p_{\mathrm{T}})/v_3(p_{\mathrm{T}})$ ratios for identified particles ($\pi^{\pm}, K^{\pm}, K_s^0, \phi, p, \bar{p}, \Lambda$ and $\bar{\Lambda}$) from 0%–80% central Au+Au collisions at $\sqrt{s_{\mathrm{NN}}} = 200$ GeV.

C. Integrated v_2/v_3 Ratio from AMPT Model

Figure 7 shows the AMPT calculation for the integrated v_2/v_3 ratio for identified particles from 0%–80% central Au+Au collisions at $\sqrt{s_{\mathrm{NN}}} = 39$ and 200 GeV. The integration region is limited to $1.5 < p_{\mathrm{T}} < 2.8$ GeV/c to avoid the steep decrease in the differential ratio and the large error region. Please note, the triangular flow used to calculate the $v_2(p_{\mathrm{T}})/v_3(p_{\mathrm{T}})$ ratio for 1.5 mb and 3 mb parton scattering cross section are taken from 0%–60% and 0%–70% due to the event plane resolution limits, as shown in Fig. 1. The other of v_3 values are taken from 0%–80% results.
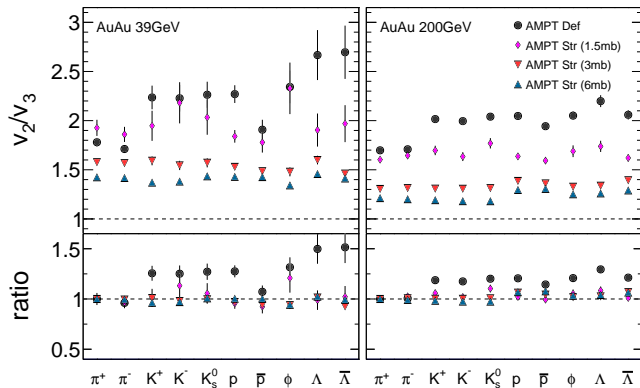
FIG. 7. (Color online) Upper panel: AMPT calculation of the integrated v_2/v_3 ratio for identified particles $(\pi^{\pm}, K^{\pm}, K_s^0, \phi, p, \bar{p}, \Lambda$ and $\bar{\Lambda})$ from 0%–80% central Au+Au collisions at $\sqrt{s_{\mathrm{NN}}} = 39$ and 200 GeV. Bottom panel: the ratio between integrated v_2/v_3 of all particles species to that of π^+

A similar anti-correlation between the integrated v_2/v_3 ratio and the parton scattering cross section is observed as in the differential $v_2(p_{\mathrm{T}})/v_3(p_{\mathrm{T}})$ ratio: the larger the parton scattering cross section, the smaller the integrated v_2/v_3 ratio. In addition, for the same parton scattering cross section, an energy dependence is observed: the lower the energy the larger the integrated v_2/v_3 ratio. We further observe that the integrated v_2/v_3 ratio calculated by string melting AMPT shows no mass (particle type) dependence, the ratio between integrated v_2/v_3 of all particle species to that of π^+ are consistent with 1 within 10%. On the other hand the ratios of $\pi^{\pm}$ from default AMPT are lower than the rest of the particle species at both $\sqrt{s_{\mathrm{NN}}} = 39$ and 200 GeV. This indicates that the quark coalescence mechanism might play an important role in flattening the v_2/v_3 ratio. The no mass (particle type) dependence of the v_2/v_3 ratio was predicted by viscous hydrodynamics, for fast particles (particles with large p_{T}). The v_2/v_3 ratio is constant and does not depend on the mass of the particle [23]. Based

on the viscous hydrodynamics in Ref. [23], the collective flow depends on dissipative contributions and the Fourier coefficient (V_n) of the flow velocity distribution relative to the event plane, the dissipative contributions cancelled each other in v_2/v_3 ratio calculation and only V_2/V_3 left which does not depend on the mass of different particle species. Since the parton scattering cross section is related to the viscosity in hydrodynamics, the magnitude of the v_2/v_3 ratio might be usable to quantify the viscosity of the system.

IV. SUMMARY

The AMPT calculations of elliptic flow at $\sqrt{s_{\mathrm{NN}}} = 11.5$, 39 and 200 GeV and triangular flow at $\sqrt{s_{\mathrm{NN}}} = 200$ GeV of identified particles $(\pi^{\pm}, K^{\pm}, p, \bar{p}$ and $\phi)$ from 0%–80% central Au+Au collisions were presented. Most of results from experiments can be reproduced with a parton scattering cross section between 1.5 and 3 mb by following the same analysis method as used in the experiments. An anti-correlation between the parton scattering cross section for both the differential and integrated v_2/v_3 ratio is observed. This is due to a different sensitivity of v_2 and v_3 to the parton scattering cross section. A mass (particle type) independence of the integrated v_2/v_3 ratio is observed from string melting AMPT, but not for the default AMPT. The no mass (particle type) dependence of the v_2/v_3 ratio also can be understood in the viscous hydrodynamic framework. Latter one suggests that the magnitude of the ratio might be used to quantify the viscosity of the system.

[1] S. A. Voloshin, A. M. Poskanzer, and R. Snellings, (2008), arXiv:0809.2949 [nucl-ex].

[2] P. Sorensen, (2009), arXiv:0905.0174 [nucl-ex].

[3] J. Adams *et al.* (STAR), Nucl.Phys. **A757**, 102 (2005), arXiv:nucl-ex/0501009 [nucl-ex].

[4] K. Adcox *et al.* (PHENIX), Nucl.Phys. **A757**, 184 (2005), arXiv:nucl-ex/0410003 [nucl-ex].

[5] C. Adler *et al.* (STAR), Phys.Rev.Lett. **87**, 182301 (2001), arXiv:nucl-ex/0107003 [nucl-ex].

[6] J. Adams *et al.* (STAR), Phys.Rev.Lett. **92**, 052302 (2004), arXiv:nucl-ex/0306007 [nucl-ex].

[7] P. Huovinen, P. Kolb, U. W. Heinz, P. Ruuskanen, and S. Voloshin, Phys.Lett. **B503**, 58 (2001), arXiv:hep-ph/0101136 [hep-ph].

[8] D. Molnar and S. A. Voloshin, Phys.Rev.Lett. **91**, 092301 (2003), arXiv:nucl-th/0302014 [nucl-th].

[9] J. Adams *et al.* (STAR), Phys.Rev.Lett. **95**, 122301 (2005), arXiv:nucl-ex/0504022 [nucl-ex].

[10] B. Abelev *et al.* (STAR), Phys.Rev.Lett. **99**, 112301 (2007), arXiv:nucl-ex/0703033 [NUCL-EX].

[11] B. Abelev *et al.* (STAR), Phys.Rev. **C81**, 044902 (2010), arXiv:1001.5052 [nucl-ex].

[12] B. Abelev *et al.* (STAR), Phys.Rev. **C75**, 054906 (2007), arXiv:nucl-ex/0701010 [nucl-ex].

[13] L. Adamczyk *et al.* (STAR), Phys.Rev.Lett. **110**, 142301 (2013), arXiv:1301.2347 [nucl-ex].

[14] L. Adamczyk *et al.* (STAR Collaboration), Phys.Rev. **C88**, 014902 (2013), arXiv:1301.2348 [Unknown].

[15] B. Alver and G. Roland, Phys.Rev. **C81**, 054905 (2010), arXiv:1003.0194 [nucl-th].

[16] D. Teaney and L. Yan, Phys.Rev. **C83**, 064904 (2011), arXiv:1010.1876 [nucl-th].

[17] B. H. Alver, C. Gombeaud, M. Luzum, and J.-Y. Ollitrault, Phys.Rev. **C82**, 034913 (2010), arXiv:1007.5469 [nucl-th].

[18] R. S. Bhalerao, M. Luzum, and J.-Y. Ollitrault, Phys.Rev. **C84**, 034910 (2011), arXiv:1104.4740 [nucl-th].

[19] L. Adamczyk *et al.* (STAR), Phys.Rev. **C88**, 014904 (2013), arXiv:1301.2187 [nucl-ex].

[20] X. Sun (STAR Collaboration), Nucl.Phys. **A931**, 1194 (2014).

[21] E. Retinskaya, M. Luzum, and J.-Y. Ollitrault, Phys.Rev. **C89**, 014902 (2014), arXiv:1311.5339 [nucl-th].

[22] E. Retinskaya, M. Luzum, and J.-Y. Ollitrault, Nucl.Phys. **A926**, 152 (2014), arXiv:1401.3241 [nucl-th].

[23] C. Lang and N. Borghini, Eur.Phys.J. **C74**, 2955 (2014), arXiv:1312.7763 [nucl-th].

[24] A. M. Poskanzer and S. Voloshin, Phys.Rev. **C58**, 1671 (1998), arXiv:nucl-ex/9805001 [nucl-ex].

[25] S. Voloshin and Y. Zhang, Z.Phys. **C70**, 665 (1996), arXiv:hep-ph/9407282 [hep-ph].

[26] K. Xiao, N. Li, S. Shi, and F. Liu, J.Phys. **G39**, 025011 (2012), arXiv:1111.6213 [nucl-th].

[27] D. Kharzeev and M. Nardi, Phys.Lett. **B507**, 121 (2001), arXiv:nucl-th/0012025 [nucl-th].

[28] Z.-W. Lin, C. M. Ko, B.-A. Li, B. Zhang, and S. Pal, Phys.Rev. **C72**, 064901 (2005), arXiv:nucl-th/0411110 [nucl-th].

[29] M. Gyulassy and X.-N. Wang, Comput.Phys.Commun. **83**, 307 (1994), arXiv:nucl-th/9502021 [nucl-th].

[30] X.-N. Wang, Phys.Rev. **D43**, 104 (1991).

[31] X.-N. Wang and M. Gyulassy, Phys.Rev. **D44**, 3501 (1991).

[32] B. Zhang, Comput.Phys.Commun. **109**, 193 (1998), arXiv:nucl-th/9709009 [nucl-th].

[33] B. Li and W. Bauer, Phys.Rev. **C44**, 450 (1991).

[34] B.-A. Li and C. M. Ko, Phys.Rev. **C52**, 2037 (1995), arXiv:nucl-th/9505016 [nucl-th].

[35] Z.-w. Lin and C. Ko, Phys.Rev. **C65**, 034904 (2002), arXiv:nucl-th/0108039 [nucl-th].

[36] L.-W. Chen, C. Ko, and Z.-W. Lin, Phys.Rev. **C69**, 031901 (2004), arXiv:nucl-th/0312124 [nucl-th].

[37] J. Xu and C. M. Ko, Phys.Rev. **C84**, 014903 (2011), arXiv:1103.5187 [nucl-th].

[38] S. Adler *et al.* (PHENIX), Phys.Rev.Lett. **91**, 182301 (2003), arXiv:nucl-ex/0305013 [nucl-ex].

[39] J.-Y. Ollitrault, A. M. Poskanzer, and S. A. Voloshin, Phys.Rev. **C80**, 014904 (2009), arXiv:0904.2315 [nucl-ex].

[40] M. Gyulassy, Y. Pang, and B. Zhang, Nucl.Phys. **A626**, 999 (1997), arXiv:nucl-th/9709025 [nucl-th].

[41] B. Zhang, M. Gyulassy, and C. M. Ko, Phys.Lett. **B455**, 45 (1999), arXiv:nucl-th/9902016 [nucl-th].